Design Constraints and Reconstruction Algorithms for Traverse-Continuous-Rotate CT Scanners

DAVID NAHAMOO, CARL R. CRAWFORD, AND AVINASH C. KAK, MEMBER, IEEE

Abstract—In this paper a new configuration for a computerized tomographic (CT) scanner is presented. The machine is essentially a hybrid combination of second- and third-generation scanners. A single source of X-rays and an array of detectors are mounted on a gantry. The source/detector array grouping traverses the object while the gantry *continuously* rotates around the object. Conditions will be derived so that the projection data will completely cover the Radon space *without any holes or partial overlaps*, thus ensuring the existence of efficiently implementable reconstruction algorithms for inverting the data. We will also present a new convolution-backprojection algorithm for reconstructing tomographic images from data generated on such a scanner.

I. INTRODUCTION

IN the evolution of computerized tomography (CT), one can see a pattern of machines with increasing resolution and decreasing data acquisition and reconstruction times [1]. These improvements have not come about without some negative aspects. The current third- and fourth-generation machines are far more complex and much more costly than the original first- and second-generation machines.

Perhaps the most significant improvements in CT imaging took place when the transition was made from the second- to the third-generation scanners. In a second-generation scanner, a narrow-angle source fan illuminates a small number of detectors, as shown in Fig. 1(a). This source-detector combination makes a linear traverse, as shown in the figure, thereby generating simultaneously as many projections as the number of detectors used. At the end of each traverse, the gantry supporting the source and the detectors rotates to another angular position around the object, and the translation is repeated to generate another set of parallel projections. The translate-rotate movements are repeated until sufficient data are collected. Since only a small number of detectors and associated electronics (sample and hold, and digitization) are used, such machines are not very expensive. However, due to mechanical limitations, their data acquisition times are relatively long. In both the rotate and traverse situations a large mass must be accelerated and brought back to rest. This puts a limitation on the maximum traverse and rotation velocities.

On the other hand, in a third-generation scanner [see Fig. 1(b)], a wide-angle source fan is used to illuminate an array that may contain as many as 1000 detectors. The object cross section to be imaged is contained completely within the source

fan. During the continuous rotation of the gantry supporting the source and the detectors around the object, fan-beam projections are taken in a very short time. The price paid, however, is the very large number of detectors used and the associated electronics, which are largely responsible for the high cost of such machines.

In this paper we propose a new scan configuration which has the potential of leading to a low cost body scanner. The proposed machine is essentially a hybrid combination of the second- and the third-generation scanners. The data acquisition time for this machine should be much less than that for the second-generation scanners, and the cost should be intermediate between a second- and a third-generation scanner since only a few detectors are used.[1]

As in a second-generation machine, the proposed scanner also uses a partial fan, albeit it is now wider. The source-detector combination performs linear traverses, again as in the second-generation machine. However, the gantry supporting the source-detector hardware now rotates continuously regardless of the traverses. Thus, the term "continuous rotate" is applied to this configuration.

In this paper we have first derived the fundamental conditions that must be satisfied by a traverse-continuous-rotate-type CT scanner. These conditions are necessary for the existence of efficiently implementable reconstruction algorithms. Basically, these conditions state that as long as certain periodicity conditions are satisfied, the traverse and the rotation can be arbitrary functions of time. *These conditions ensure that the Radon space is filled up without any holes or partial overlaps.* We have also presented a design equation that explicitly brings out the dependence of angle of the source fan on the ratio of the reverse-traverse to forward-traverse velocities.

This paper also presents the theoretical development of a new convolution-backprojection algorithm for traverse-continuous-rotate scanners. Although the filter function used in this algorithm is the same as for the third-generation fan-beam scanners [2], [3], the weighting function for the projec-

[1] One could say that the main thrust of this paper lies in our showing that in a second-generation machine, the rotation of the source-detector gantry does *not* have to be discrete. If a second-generation scanner were to be designed with the same source-fan angle as in the configuration proposed here, the data acquisition times would become comparable. So far, however, all the second-generation scanners have had a very small source-fan angle. Compared to such scanners, the proposed machine would be much faster. (Also note that since the source-detector gantry has considerable mass, it is believed that the mechanical design of a second-generation scanner would be much simplified if the gantry did not have to be rotated in precise discrete steps.)
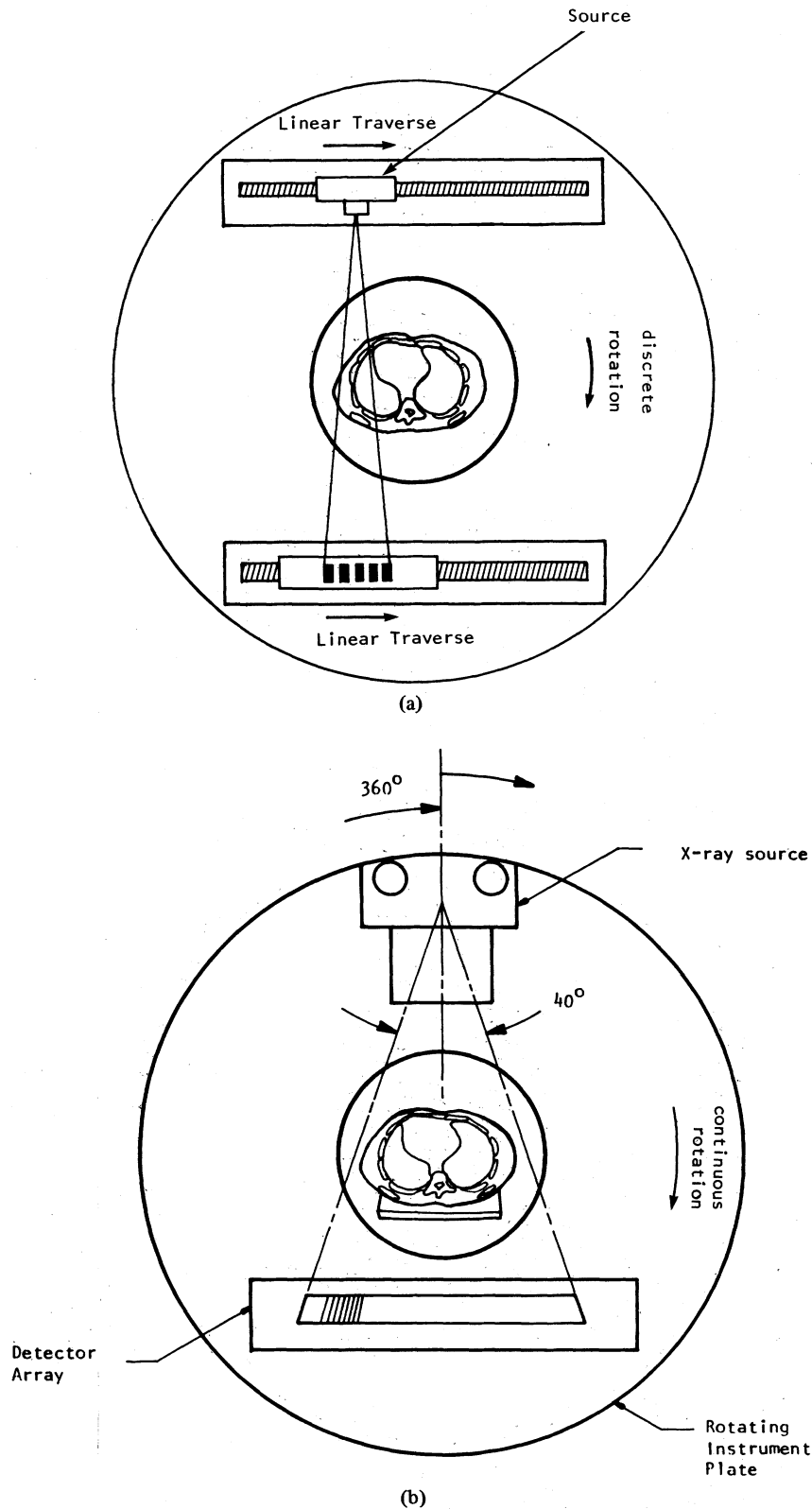
Fig. 1. (a) In a second-generation machine, a narrow angle fan illuminates a small number of detectors. (b) In a third-generation scanner, a wide angle fan is used to illuminate the entire cross section.

tion data is different. We will also show that the point spread function of the backprojection operator is $1/r$. This implies that if for some reason one did not want to use the convolution-backprojection algorithm, the reconstructions may still be obtained by post-filtering the backprojection of the measured data.

II. THE NECESSARY CONDITIONS

Since the discussion here is presented in terms of the Radon space, it will first be defined. In Fig. 2(a) is shown an object $f(x, y)$ which may represent a cross section of a human body. A line, such as AB shown in Fig. 2(a), is called a *ray*. The
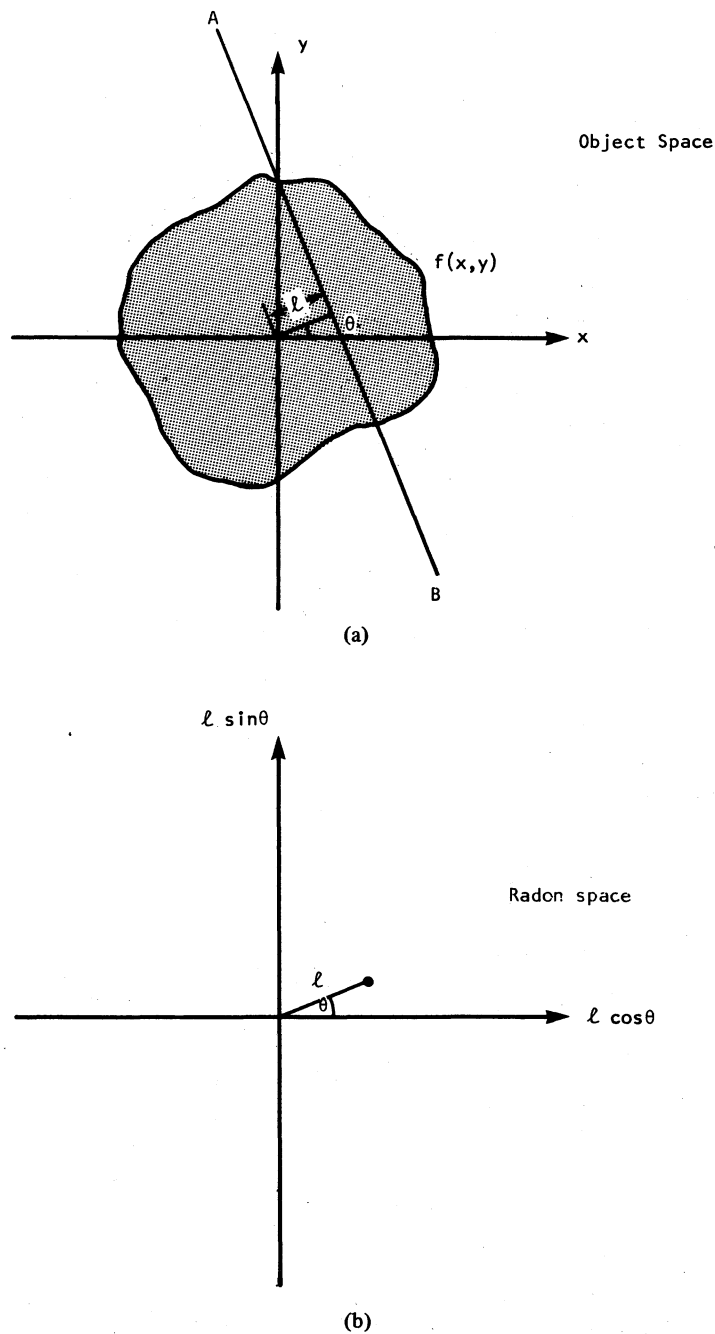
Fig. 2. (a) The function $f(x, y)$ represents a cross section whose tomographic image is sought. (b) In the Radon space, the ray integral along the line AB is represented by the value given to a single point with polar coordinates (l, θ).

integral of $f(x, y)$ along a ray is called a *ray integral*. The location of a ray is determined by the two parameters l and θ shown in Fig. 2(a). The Radon space is the $(l \cos \theta, l \sin \theta)$ plane shown in Fig. 2(b). In this space the ray integral is represented by the value of a two-dimensional function at a single point, whose polar coordinates are (l, θ).

Assume that the object in Fig. 2(a) can be completely contained within a circle of radius R. This circle will be called the "object circle." It is known that the object can be perfectly reconstructed from its projection data provided the Radon space is completely filled, without any holes or partial overlaps, within a circular domain of radius R [see Fig. 3(a)] [4],

[5].[2] In order for this to be true, we will, in this section, derive the conditions that must be satisfied by a traverse-continuous-rotate machine.

Although, in this paper, we use the polar coordinate representation of the Radon space as shown in Fig. 2(b), one may

[2]The circular domain of radius R in the Radon space will also be referred to as the Radon disk.

Our statement here should not be construed to imply that the filling of the Radon disk without any holes or partial overlaps is always a *necessary* condition for perfect reconstructability. However, it is a *sufficient* condition. This follows from the inverse Radon transform relationship.
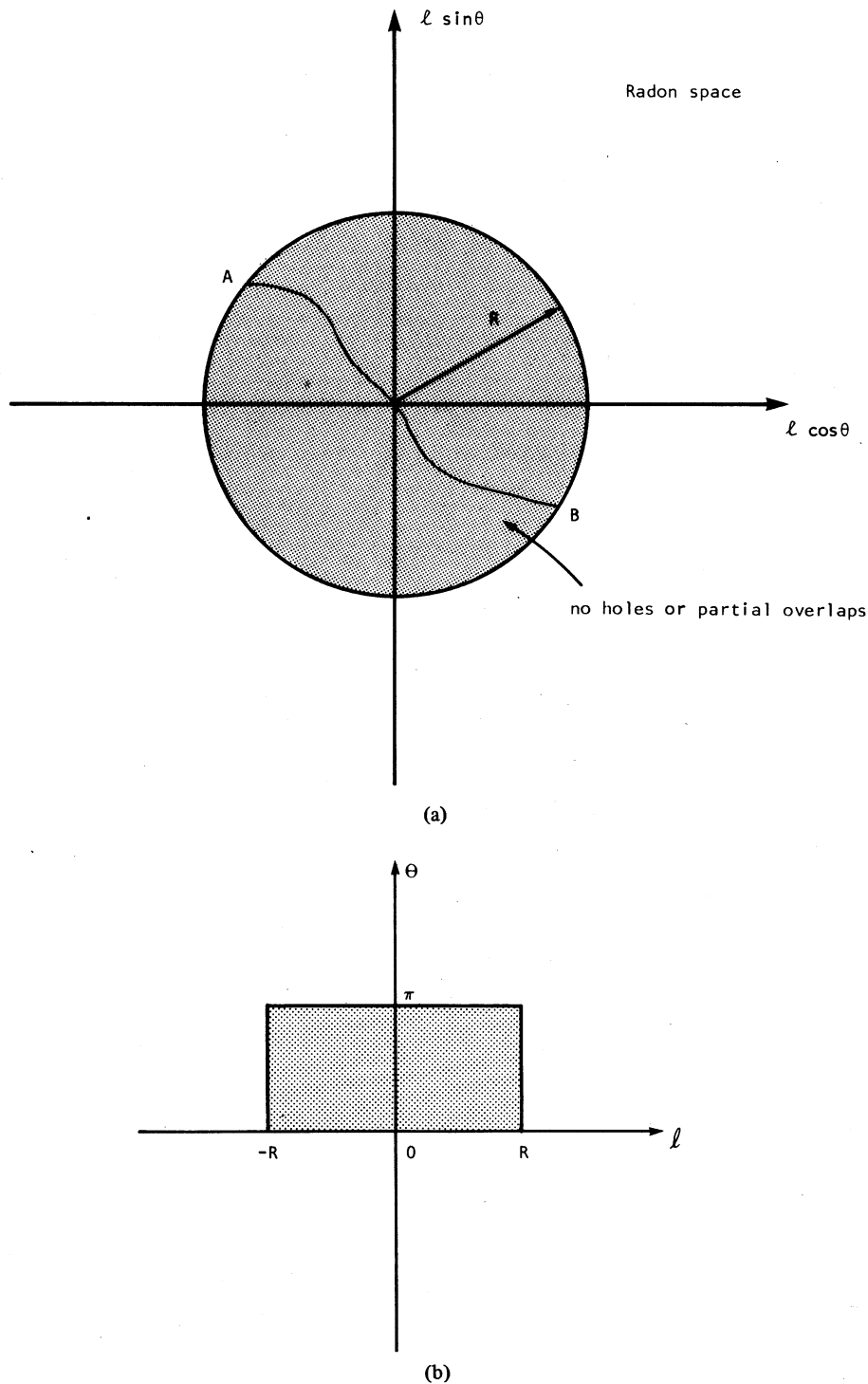
(a)

(b)

Fig. 3. (a) This figure shows the case when the projection data com-
pletely fills up a circle of radius R in the Radon space. In this case,
any object that can be contained within a circle of radius R can be
reconstructed perfectly. (b) An alternate representation of the Radon
space with l and θ as Cartesian coordinates.

also use the Cartesian coordinate representation shown in
Fig. 3(b), in which l and θ are, respectively, the horizontal and
the vertical coordinates. In this representation, for perfect
reconstruction of an object contained within a circle of
radius R, the sufficient condition is to fill up the shaded region
in Fig. 3(b) without any holes or partial overlaps.

Comparing the polar [see Fig. 3(a)] and the rectangular [see

Fig. 3(b)] representations, note that the origin in the former is
a point of singularity. That is due to the fact that *all* the points
on the line $l = 0$ in Fig. 3(b) collapse into a single point at the
origin in Fig. 3(a). Therefore, a single-valued continuous
function in Fig. 3(b) will be multiple valued at the origin in
Fig. 3(a). The origin in Fig. 3(a) being a point of singularity is
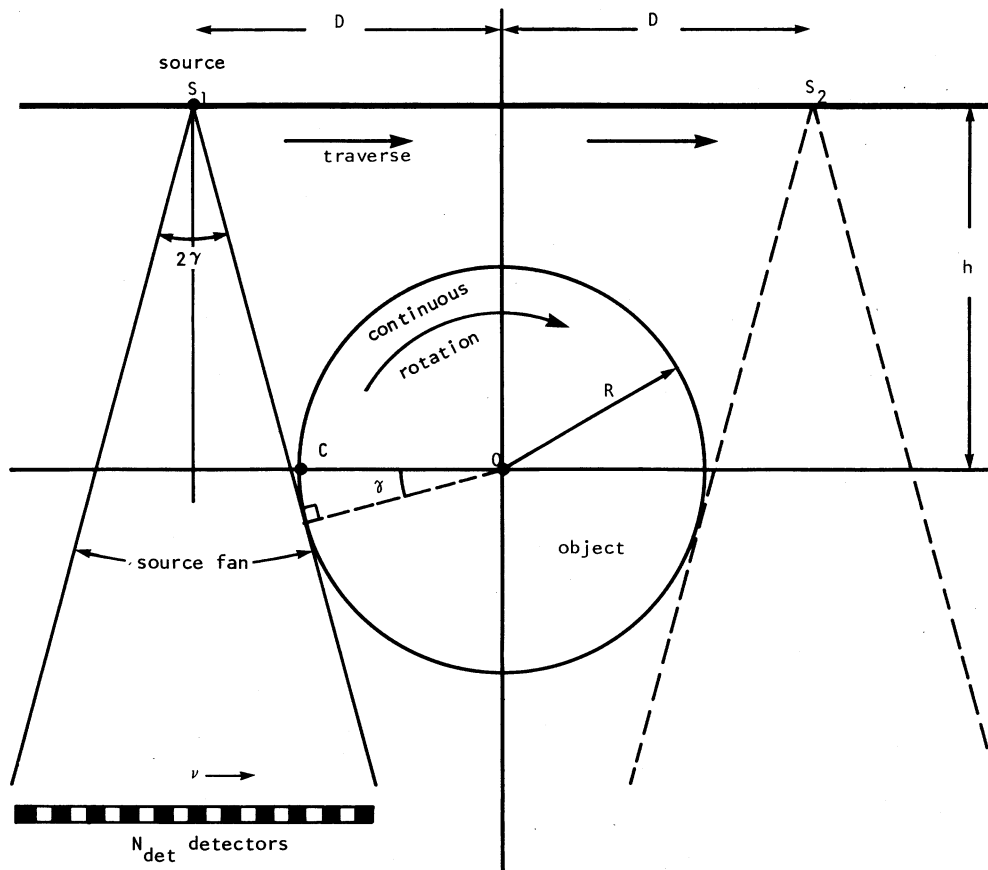not a matter of grave concern because in this report, when we

Fig. 4. The source traverses linearly between S_1 and S_2, while the gantry supporting the traversing source-detector system rotates continuously around the object. For mathematical purposes, one can consider the gantry to be stationary while the object is assumed to be rotating continuously in the opposite direction.

talk about filling up the Radon disk, we will do so by "sweeping" the disk with contours which pass through the origin, as opposed to filling up the disk with individual points. Consider, for example, an arbitrary contour AB shown in Fig. 3(a). Associated with this contour is a unique value at the origin, for which $l = 0$, and θ corresponds to the tangent to the contour there. If the Radon disk were to be filled up with circular sweeps of the contour AB (*the contour itself may undergo continuous and periodic deformations during the sweep*), for each rotational position of the contour there would correspond a unique value of (l, θ) at the origin.

In a traverse-continuous-rotate-type machine, the source detector system traverses as in a second-generation CT scanner. While this traverse is taking place, the gantry supporting the source and the detectors continuously rotates around the object. For mathematical purposes, the rotation of the gantry is exactly equivalent to the object rotating continuously in the opposite direction while the source-detector system traverses back and forth on a fixed gantry, as shown in Fig. 4.

During traverses, the source is considered to be at its beginning position when the right extreme ray of the source fan is tangential to the object circle, as depicted by position S_1 in Fig. 4. Similarly, the source will be considered to be at the end of its traverse, as shown by position S_2, when the left extreme ray

in the source fan becomes tangential to the object circle after the source fan has exited the object circle. Let $2D$ be the total distance between the beginning and the end positions. Using Fig. 4, it can easily be shown that

$$D = \frac{R + h \sin \gamma}{\cos \gamma} \tag{1}$$

where h is the perpendicular distance between the center of rotation and the traverse line and 2γ is the source-fan angle.

We will now use $S(t)$ to denote the traverse motion as a function of time. Also, let $\alpha(t)$ denote the angle through which the object has rotated in time t. At some time t, the source and the object may appear as shown in Fig. 5. Note that the reference point C on the object circle in Fig. 4 has now rotated through an angle $\alpha(t)$, while the source is at the lateral distance $S(t)$. Let us consider a ray SA in the source fan subtending an angle β with the vertical. The Radon space (l, θ) representation of this ray is given by

$$\theta = \alpha(t) + \beta$$

$$l = h \sin \beta + S(t) \cos \beta. \tag{2}$$

Constraints will now be derived on $\alpha(t)$, $S(t)$, h, and γ, so that the Radon space is completely filled without any holes or
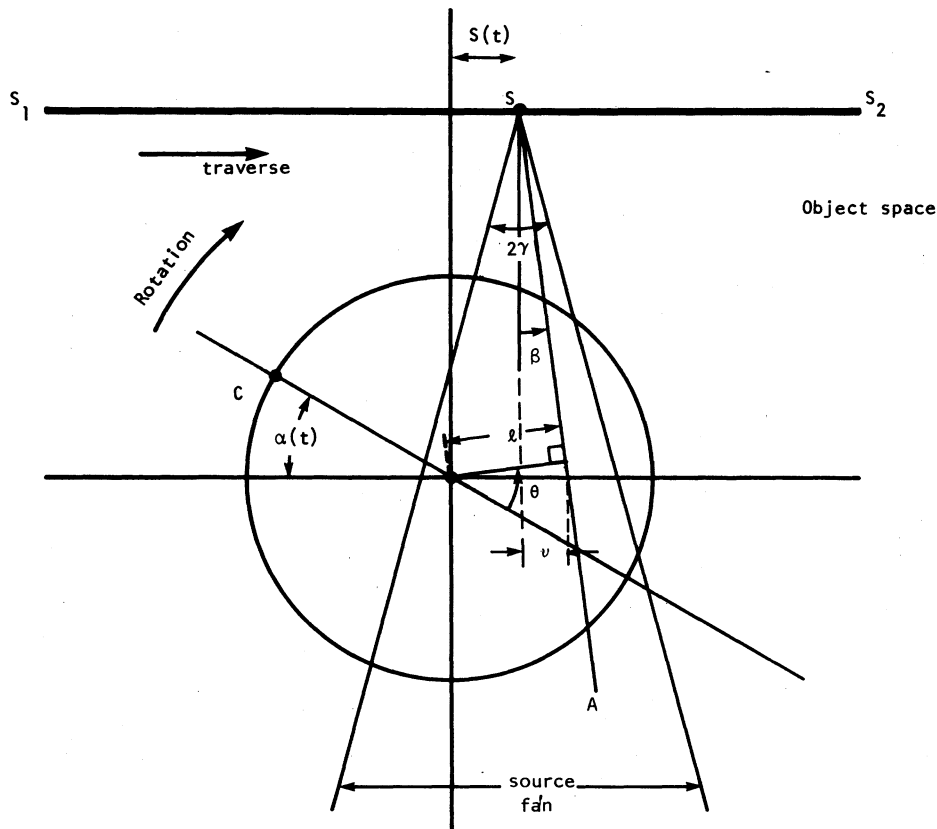
Fig. 5. The geometrical relationship between (α, β) coordinates and the
Radon (l, θ) coordinates is shown.

partial overlaps. In order to do so, let us first examine the "track" generated in the Radon space by the extreme right ray of the source fan as it traverses from left to right. This track is shown in Fig. 6 by the heavy solid line inside the Radon space circle. The curvature of this track depends upon the relationship between the rotation function $\alpha(t)$ and the translation function $S(t)$. If there is no rotation during the traverse, the curvature disappears and the track becomes a straight line passing through the origin. The dashed line inside the circle is the track generated by the left extreme ray. It is easily shown that any source ray between the left and the right extremes will generate a track that would lie between the heavy solid and the dashed lines within the circle in Fig. 6. Therefore, as the source completes one traverse, the region of Radon space that it will cover will be as shown in Fig. 7.

As shown in Fig. 7, the Radon space tracks generated by the extreme left and right rays will be denoted by g_L^i and g_R^i, $i = 1, \cdots, N$ respectively. The superscript i signifies the ith traverse. In general, the region of the Radon space covered in the $(i + 1)$st traverse will be as shown in Fig. 8 for clockwise rotation.[3] Therefore, if we want to avoid holes (blank spaces) and partial overlaps between regions covered in successive traverses, the following condition must be satisfied:

$$g_R^i = g_L^{(i+1)}. \tag{3}$$

We will now translate (3) into conditions on rotational and

traversal velocities. In order to do so, we first need to introduce some time constants associated with the scanning system. An important constant associated with the system is the time it takes for the source to traverse from its beginning position at S_1 to the position at S_3 where the extreme left ray becomes tangential to the object circle (see Fig. 9). We will denote this time by T. The time taken by the source to traverse from S_1 to S_4, which is the position when the extreme right ray again becomes tangential to the object circle, will be denoted by T_1. The time taken by the source to traverse from the beginning position to the end position at S_2 will be denoted by T_f. If T_r is the time for the source to return to its original position at S_1 (no data are taken during the return), the total time associated with one traverse will be $T_f + T_r$. This will be denoted by T_t.

As a source ray, subtending an angle β with the vertical, traverses from left to right, the values of θ and l at different times for this ray are given by (2). For the ith traverse, let these functions for the extreme left ray be denoted by $\theta_L^i(t)$ and $l_L^i(t)$, respectively. The corresponding quantities for the extreme right ray will be denoted by $\theta_R^i(t)$ and $l_R^i(t)$, respectively. Using (2) and substituting $\beta = -\gamma$ for the leftmost ray and $\beta = +\gamma$ for the rightmost ray, we get

$$g_R^i \quad \begin{cases} \theta_R^i(t) = \alpha(t) + \gamma \\ l_R^i(t) = h \sin\gamma + S(t)\cos\gamma, \end{cases}$$

$$(i - 1)T_t \leqslant t < (i - 1)T_t + T_1 \tag{4}$$

and

[3]Unless otherwise mentioned we will consider only the case of clockwise rotation.
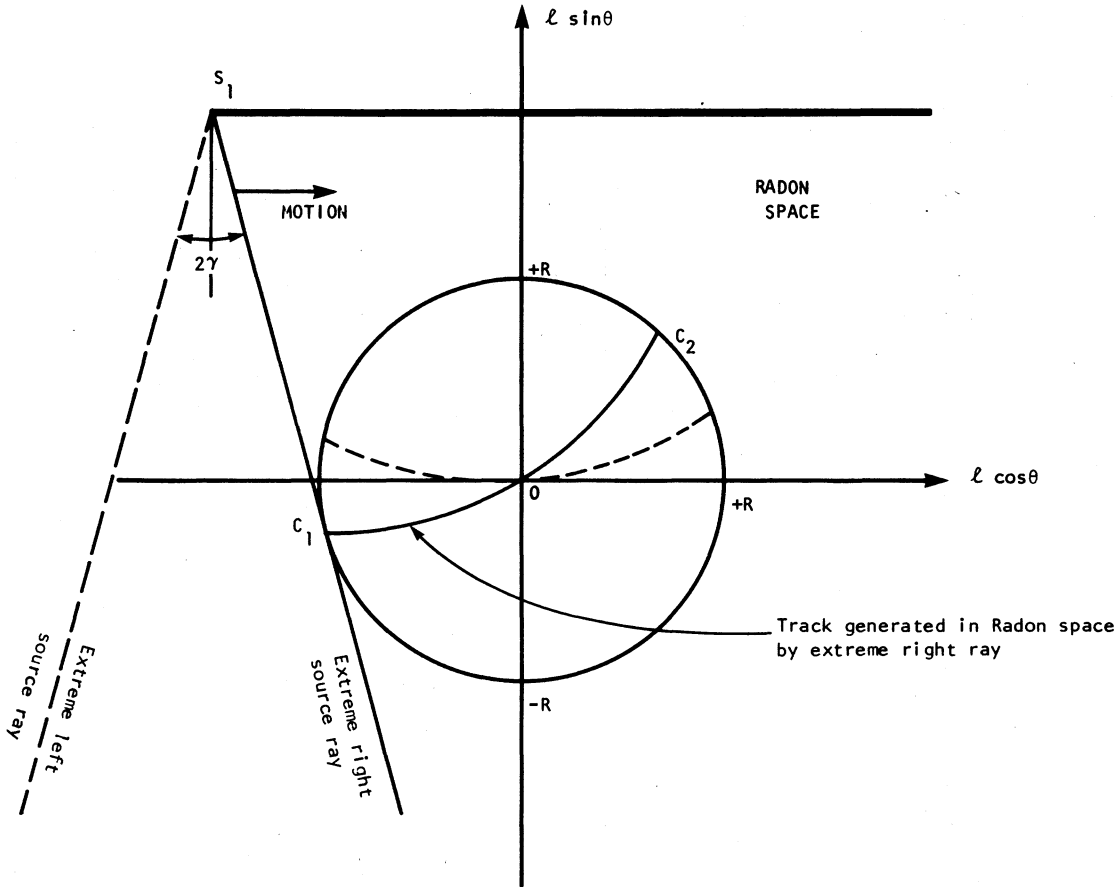
Fig. 6. The tracks generated in the Radon space by the extreme left and right source-fan rays are shown. Strictly speaking, the presentation in the figure of the extreme left and right rays is unjustified, since the figure depicts the Radon space. The presence of these rays here is merely symbolic and illustrates their association with the corresponding tracks within the Radon disk.

$$g_L^{(i+1)} \begin{cases} \theta_L^{(i+1)}(t) = \alpha(t) - \gamma \\ l_L^{(i+1)}(t) = -h \sin \gamma + S(t) \cos \gamma, \end{cases}$$

$$iT_t + T \leqslant t < iT_t + T_f. \quad (5)$$

To satisfy (3) the expressions in (4) must be set equal to the corresponding ones in (5), after we allow for the fact that the tracks g_R^i and $g_L^{(i+1)}$ are not generated at the same time. Suppose the first point (point C_1 in Fig. 8) on the g_R^i track is generated at t_1. It is easy to see that the first point (point C_2 in Fig. 8) on the $g_L^{(i+1)}$ track will be generated at a time $t_1 + T_t + T$. The symbolic equality in (3) therefore implies

$$\theta_R^i(t) = \theta_L^{(i+1)}(t + T_t + T)$$

$$l_R^i(t) = l_L^{(i+1)}(t + T_t + T),$$

$$(i-1)T_t \leqslant t < (i-1)T_t + T_1. \quad (6)$$

Substituting (4) and (5) in (6), we get

$$\alpha(t + T_t + T) - \alpha(t) = 2\gamma$$

$$S(t + T_t + T) - S(t) = 2h \tan \gamma. \quad (7)$$

The equations in (7) are the necessary conditions that must be satisfied by a traverse continuous rotate scanner. These conditions only guarantee that between successive traverses holes will not be left in the Radon space. We will now derive another condition which, when satisfied, results in no holes or partial overlaps in the Radon space between the first and the last traverses.

For ease of diagrammatic representation, we will assume that we are using only half the data collected in each traverse—the half corresponding to a region OC_1D_1—and ignoring the half corresponding to OE_1F_1 (see Fig. 8). It is clear that no holes or partial overlaps will be generated between the first and the last traverse coverages in the Radon space if

$$g_R^N = g_L^1. \quad (8)$$

If we include the half of the data that was ignored, every point in the Radon space will be covered twice when (7) and (8) are satisfied, which still precludes any *partial* overlaps.

III. NECESSARY CONDITIONS FOR THE CASE OF CONSTANT TRAVERSE AND ROTATION SPEEDS

It is inconceivable that in practice the translation motion will be different from traverse to traverse. Therefore, the function $S(t)$ may be assumed to be periodic with period T_t. That is,
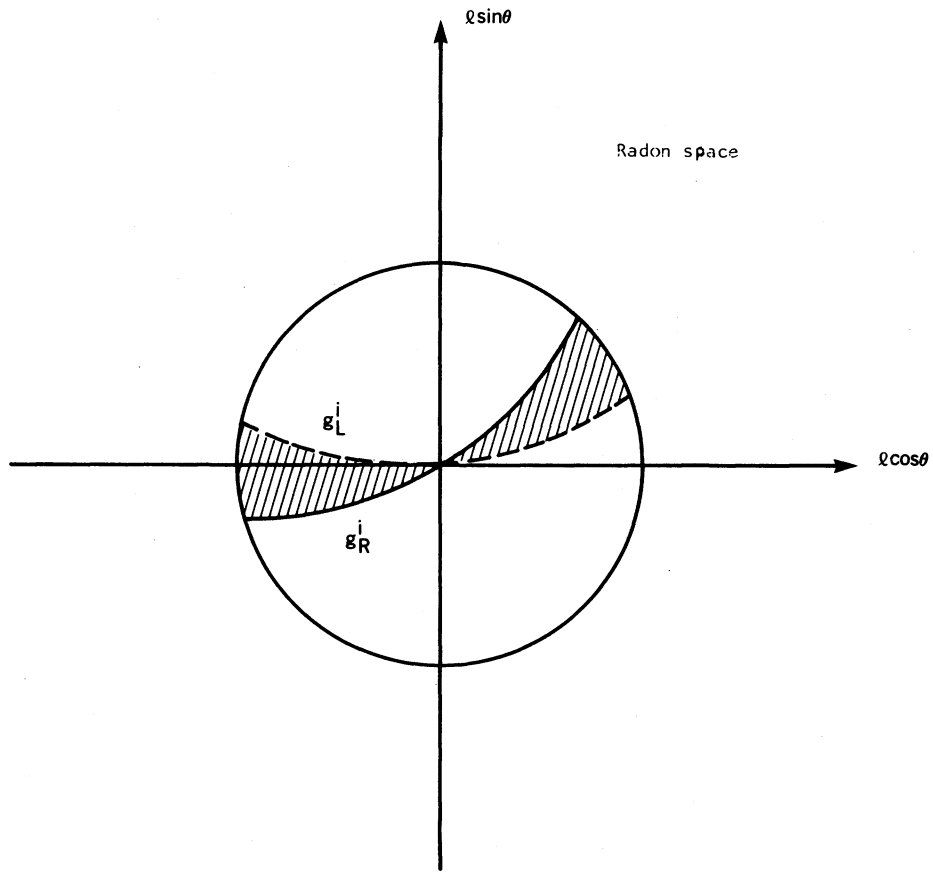
$$S(t + T_t) = S(t). \quad (9)$$

Fig. 7. As the source makes one forward traverse from left to right, the region covered in the Radon space is shown shaded here.
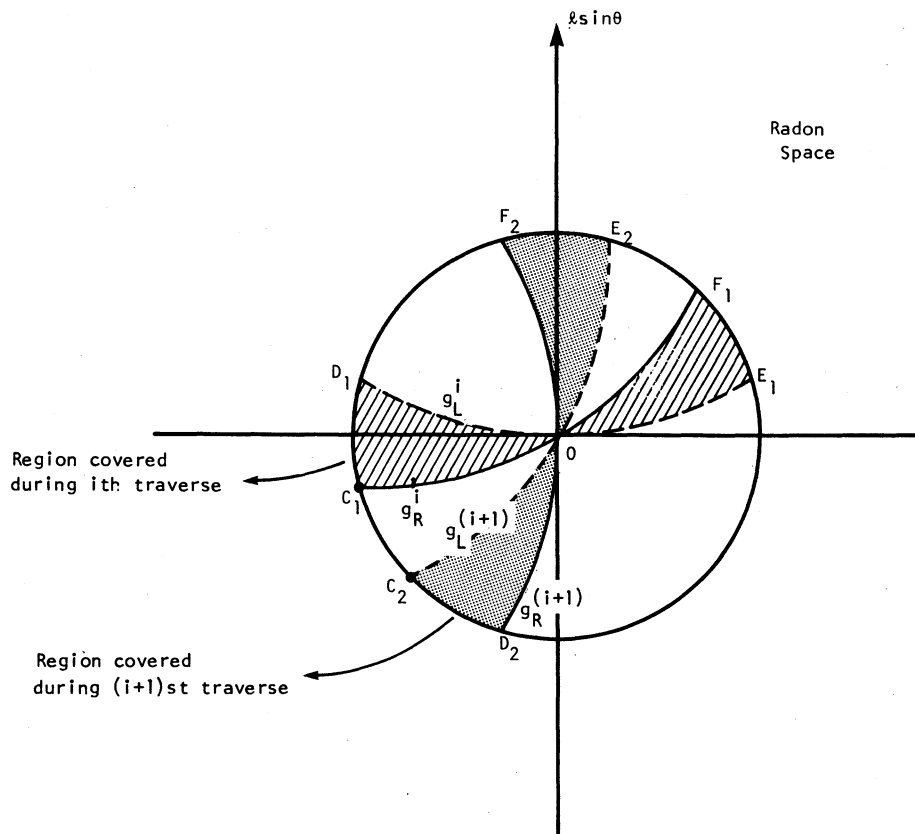

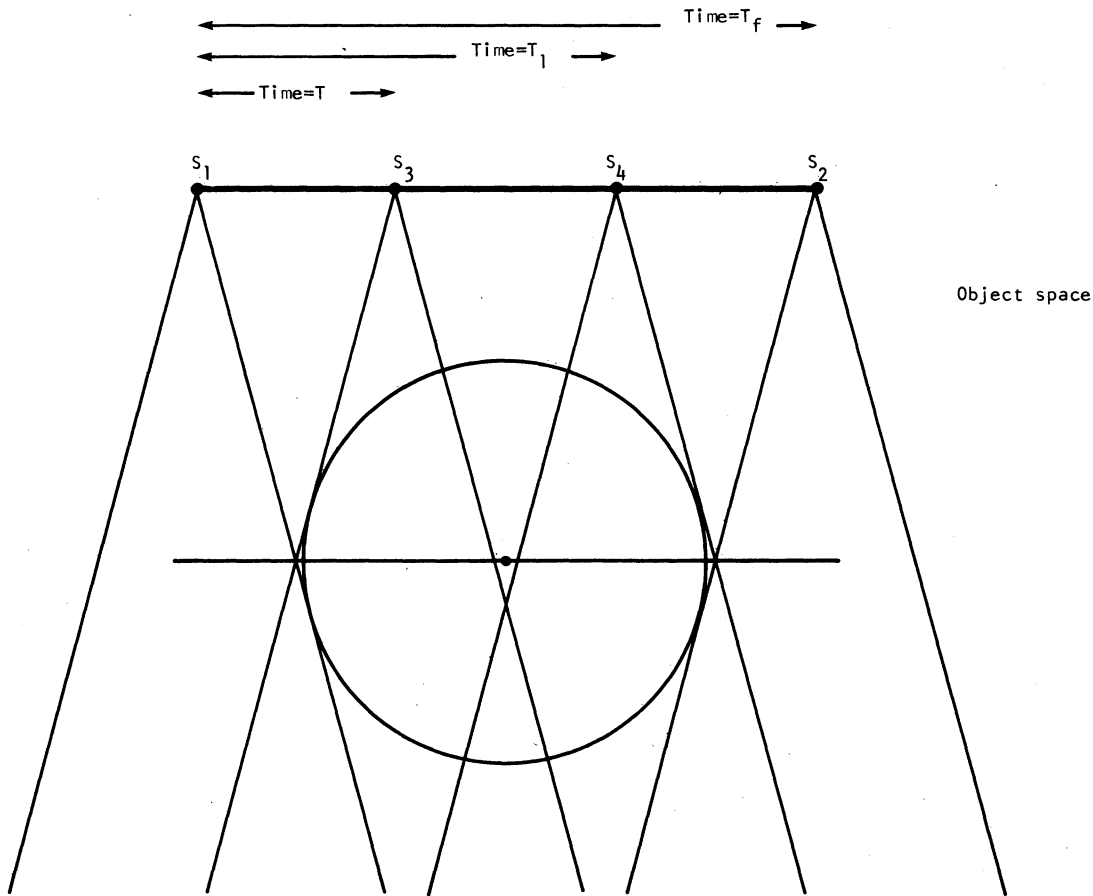Fig. 8. Regions covered in Radon space during two successive traverses for clockwise rotation.

Fig. 9. This figure shows the different time constants that can be associated with the system. T denotes the time taken for the extreme left ray to become tangential to the object circle. T_1 and T_f are similarly defined.

The same should be true for the rotation function $\alpha(t)$, except that due to the rotation occurring continuously in only one direction, there is a cumulative component in this function. The periodicity properties of $\alpha(t)$ may therefore be expressed as

$$\alpha(t + T_t) = \alpha(t) + \alpha_0 \tag{10}$$

where α_0 is the angle through which the object rotates in period T_t. Substituting (9) and (10) in (7), we get

$$\alpha(t + T) - \alpha(t) = 2\gamma - \alpha_0$$

$$S(t + T) - S(t) = 2h \tan \gamma, \quad 0 \leqslant t \leqslant T_1. \tag{11}$$

As shown in Fig. 10, let ξ be the angle along the circumference of the Radon space disk that is covered during each traverse (in time T_t). If both $S(t)$ and $\alpha(t)$ are periodic as discussed above, this angle will be the same for all the traverses. The condition in (8) will be satisfied provided

$$\xi = \frac{2\pi}{N}. \tag{12}$$

A direct consequence of having to satisfy (3) is that $\xi = \alpha_0$. This follows from the fact that on the circumference of the Radon disk, the angle between g_L^i and g_L^{i+1} is α_0. On the other hand, ξ is the angle between g_L^i and g_R^i (see also Fig. 8). Since (3) has to be satisfied, the equality follows.

We will now assume that both the forward traverse velocity V_f and the angular velocity V_a are constant. In this case, $\alpha_0 = V_a T_t (= \xi)$, and $\alpha(t + T) - \alpha(t) = V_a T$. Substituting these into (11) and (12), we get

$$\gamma = \frac{\pi}{N} \left(1 + \frac{T}{T_t} \right) \tag{13a}$$

$$V_f T = 2h \tan \gamma \tag{13b}$$

$$V_a T_t = \frac{2\pi}{N}. \tag{13c}$$

These conditions must be satisfied if the Radon space is to be covered without holes or partial overlaps.

Rationale similar to the above can be developed for the case of counterclockwise rotation also. Conditions corresponding to (3) and (8) are now given by

$$g_R^{(i+1)} = g_L^i$$

$$g_R^1 = g_L^N. \tag{14}$$

For constant traverse and rotation velocities, these reduce to the following:

$$\gamma = \frac{\pi}{N} \left(1 - \frac{T}{T_t} \right) \tag{15a}$$

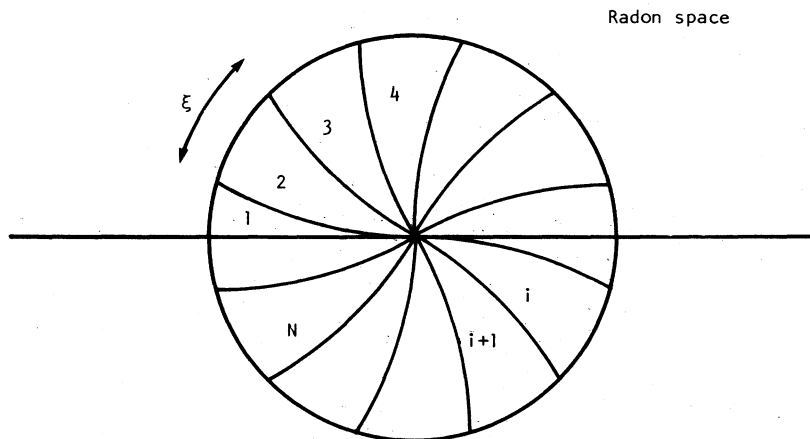$$V_f T = 2h \tan \gamma \tag{15b}$$

Radon space

Fig. 10. This figure shows that no holes will be left between the first and the last traverses provided the angle ξ is equal to $2\pi/N$ for integer N.

and

$$V_a T_t = \frac{2\pi}{N}. \qquad (15c)$$

IV. A DESIGN EQUATION

We will now present what seems like a useful design equation for traverse-continuous-rotate scanners.

For constant traverse velocities, the ratio T/T_t can be shown to be equal to (see Fig. 4)

$$\frac{T}{T_t} = \frac{2hV_r \tan \gamma}{2DV_f + 2DV_r} \qquad (16)$$

where V_f and V_r are the forward and the reverse traverse velocities. Using (1), we can write

$$\frac{T}{T_t} = \frac{kh \sin \gamma}{(R + h \sin \gamma)(1 + k)} \qquad (17)$$

where

$$k = \frac{V_r}{V_f}. \qquad (18)$$

Substituting (17) in (13a) and (15a), we obtain the following design equation:

$$\gamma = \frac{\pi}{N} \left[1 \pm \frac{kh \sin \gamma}{(R + h \sin \gamma)(1 + k)} \right]. \qquad (19)$$

For given values of h, R, N, and k, the source fan angle is the solution of this transcendental equation. The above result applies to the case of clockwise rotation with the positive sign and to the case of counterclockwise roation with the negative sign between the two terms inside the brackets.

It is interesting to examine the implications of the conditions derived in the preceding section on the mechanical parameters of the proposed scanner. The two parameters that we have looked at are the normalized machine size and the ratio of the rotational velocity to traverse velocity.

We define the normalized machine size as follows:

$$\frac{\text{machine size}}{R} = \frac{1}{R} \sqrt{[D + (h + h_d) \tan \gamma]^2 + h_d^2}. \qquad (20)$$

Machine size is meant to be the farthest point on the gantry from the center of rotation (see Fig. 11). The parameter h_d is the perpendicular distance of the detector line from the center of rotation. Substituting (1) in (20), we get the following expression:

$$\frac{\text{machine size}}{R}$$
$$= \sqrt{\left[\frac{1 + (h/R) \sin \gamma}{\cos \gamma} + (h/R + h_d/R) \tan \gamma \right]^2 + \left(\frac{h_d}{R} \right)^2}. \qquad (21)$$

The ratio of peripheral tangential velocity of the farthest point on the gantry to the forward traverse velocity is given by

$$\frac{\text{peripheral tangential velocity due to rotation}}{\text{forward traverse velocity}} = \frac{(\text{machine size}) \cdot V_a}{V_f}. \qquad (22)$$

From (13) and (15), we have $V_a = 2\gamma/(T_t \pm T)$ and $V_f = (2h \tan \gamma)/T$. Substituting these in (22) leads to the following expression:

$$\frac{\text{peripheral tangential velocity}}{\text{forward traverse velocity}} = \frac{(\text{machine size}/R)}{(T_t/T \pm 1)(h/R)} \cdot \frac{\gamma}{\tan \gamma}. \qquad (23)$$

In Table I, using (19), (21), and (23), we have shown the calculated values of the half-fan angle, normalized machine size, and the ratio of the velocities for different values of k for clockwise rotation. In these calculations we assumed that $h/R = h_d/R = 1.2$. In Table II are shown results similar to Table I, except that the rotation is now counterclockwise.

V. POINT SPREAD FUNCTION FOR THE BACKPROJECTION OPERATOR

We will now show that if the measured data are backprojected without any prefiltering, the degradation in the result-
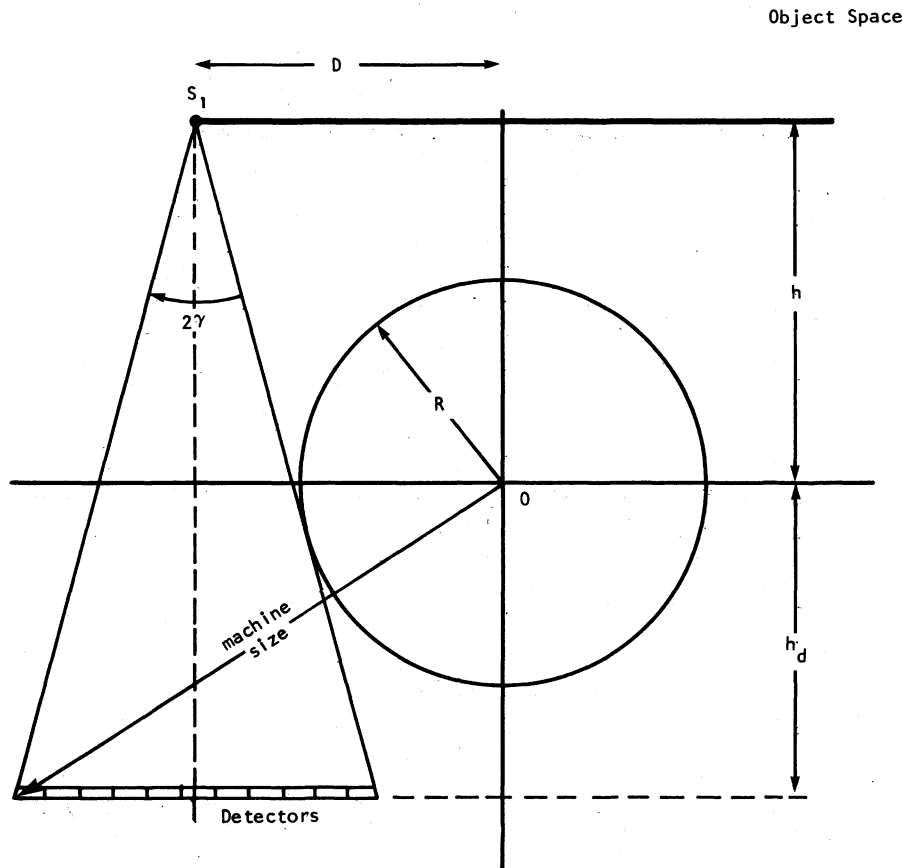
Object Space

Fig. 11. The parameter "machine size" is shown here. It is the distance of the farthest point on the gantry from the center of rotation.

TABLE I

CALCULATIONS FOR CLOCKWISE ROTATION AND $h/R = h_d/R = 1.2$. ALSO, N, THE NUMBER OF TRAVERSES, EQUALS 10

k	γ	machine size / R	peripheral tangential vel. / forward traverse vel.
.75	20.27	2.68	.24
1.00	20.68	2.71	.28
1.25	21.01	2.73	.31
1.50	21.28	2.75	.34
1.75	21.50	2.77	.36
2.00	21.69	2.78	.37

TABLE II

CALCULATIONS FOR COUNTERCLOCKWISE ROTATION AND $h/R = h_d/R = 1.2$. ALSO, N, THE NUMBER OF TRAVERSES, EQUALS 10

k	γ	machine size / R	peripheral tangential vel. / forward traverse vel.
.75	16.08	2.40	.23
1.00	15.79	2.38	.27
1.25	15.57	2.37	.30
1.50	15.39	2.36	.32
1.75	15.25	2.35	.34
2.00	15.14	2.34	.36

ing reconstruction is convolutional. The point spread function of this degradation is $1/r$, which is the same as for the existing first- through fourth-generation CT scanners [6], [7]. Our derivation is based on the transformation between (α, β) and (l, θ) spaces being regular (which implies that the transformation is one-to-one and onto). In Section VI we will prove this property, and in Section VII we will use the same property to derive a convolution-backprojection algorithm for traverse continuous rotate scanners.

A ray integral[4] is defined by the following relationship:

$$p_\theta(l) = \iint f(x,y)\, \delta(x \cos \theta + y \sin \theta - l)\, dx\, dy. \quad (24)$$

[4] Indefinite integrals have the implied limits $(-\infty, \infty)$.

The quantity $p_\theta(l)$ is the value to be assigned to the point (l, θ) in the Radon space. For traverse-continuous-rotate scanners, the rays are more conveniently characterized by (α, β) parameters presented in Section II. For each traverse there exists a one-to-one transformation between (l, θ) and (α, β) coordinates, which is given by (2). Substituting (2) in (24), we get

$$q_\alpha(\beta) = \iint f(x,y)\, \delta\, [x \cos (\alpha + \beta) + y \sin(\alpha + \beta)$$

$$- h \sin \beta - S(t) \cos \beta]\, dx\, dy \quad (25)$$

where $q_\alpha(\beta)$ represents the projection data of the traverse-continuous-rotate scanner.

Given the parallel projection data $p_\theta(l)$, the backprojection

is defined by the following integral:

$$g(x,y) = \frac{1}{2} \int_0^{2\pi} p_\theta(l)\, d\theta \qquad (26)$$

where

$$l = x \cos\theta + y \sin\theta. \qquad (27)$$

This relationship may be transformed into (α, β) coordinates by using (2), provided that the transformation is regular:

$$g(x,y) = \frac{1}{2} \int_\eta p_{\alpha+\beta}(h \sin\beta + S(t) \cos\beta)\, \frac{\partial\theta}{\partial\alpha}\, d\alpha \qquad (28)$$

where η is a contour of integration in the (α, β) plane. The following equality, which is obtained by substituting (2) in (27), defines the contour

$$\eta: x \cos(\alpha+\beta) + y \sin(\alpha+\beta) - S(t)\cos\beta - h\sin\beta = 0. \qquad (29)$$

Equation (28) may be expressed as a sum of integrals, each member of this sum performing an integration only over those values of α that are covered in one traverse:

$$g(x,y) = \frac{1}{2} \sum_{i=1}^N \int_{(i-1)\alpha_0}^{(i-1)\alpha_0 + \alpha'} q_\alpha(\beta) \left|1 + \frac{\partial\beta}{\partial\alpha}\right| d\alpha \qquad (30)$$

where α' is the range of $\alpha(t)$ covered in the forward traverse only, and is given by

$$\alpha' = V_a\, \frac{kT_t}{1+k}. \qquad (31)$$

In (30) we have also used the fact that $p_{\alpha+\beta}(h\sin\beta + S(t)\cos\beta)$ is by definition the new projection data represented by $q_\alpha(\beta)$. The values of β to be used in (30) are determined by (29). Equations (25) and (30) are by definition the projection and backprojection processes of a traverse-continuous-rotate scanner. We now want to show that $g(x,y)$ in (30) is related to $f(x,y)$ in (25) by convolution with $1/r$.

Substituting (25) in (30), we get

$$g(x,y) = \frac{1}{2} \sum_{i=1}^N \iint dx'\, dy'\, f(x',y')$$
$$\cdot \int_{(i-1)\alpha_0}^{(i-1)\alpha_0 + \alpha'} \delta[x'\cos(\alpha+\beta) + y'\sin(\alpha+\beta)$$
$$- h\sin\beta - S(t)\cos\beta] \left|1 + \frac{\partial\beta}{\partial\alpha}\right| d\alpha. \qquad (32)$$

In this integral the argument of the delta function can be simplified using (29):

$$g(x,y) = \frac{1}{2} \sum_{i=1}^N \iint dx'\, dy'\, f(x',y')$$
$$\cdot \int_{(i-1)\alpha_0}^{(i-1)\alpha_0 + \alpha'} \delta[(x'-x)\cos(\alpha+\beta)$$
$$+ (y'-y)\sin(\alpha+\beta)] \left|1 + \frac{\delta\beta}{\delta\alpha}\right| d\alpha. \qquad (33)$$

This integral may be written in the form

$$g(x,y) = \frac{1}{2} \iint dx'\, dy'\, f(x',y')$$
$$\cdot \sum_{i=1}^N \int_{(i-1)\alpha_0}^{(i-1)\alpha_0 + \alpha'} \delta[a(\alpha,\beta)] \left|1 + \frac{\partial\beta}{\partial\alpha}\right| d\alpha \qquad (34)$$

where

$$a(\alpha,\beta) = (x'-x)\cos(\alpha+\beta) + (y'-y)\sin(\alpha+\beta). \qquad (35)$$

Consider only the summation and the inner integral of (34), which may be shown to satisfy the following equality [9]:

$$\sum_{i=1}^N \int_{(i-1)\alpha_0}^{(i-1)\alpha_0 + \alpha'} \delta[a(\alpha,\beta)] \left|1 + \frac{\partial\beta}{\partial\alpha}\right| d\alpha$$
$$= \sum_{j=1}^2 \left[\frac{\left|1 + \dfrac{\partial\beta}{\partial\alpha}\right|}{\left|\dfrac{\partial a}{\partial\alpha} + \dfrac{\partial a}{\partial\beta}\dfrac{\partial\beta}{\partial\alpha}\right|} \right]_{(\alpha,\beta)=(\alpha_j,\beta_j)} \qquad (36)$$

where we have used the fact that $a(\alpha, \beta)$ is equal to zero at only two points, denoted by (α_1, β_1) and (α_2, β_2), in the (α, β) plane. This follows from the discussion in Section III where we have shown that the Radon space is covered exactly twice. Equation (36) can be further simplified by noting that

$$\frac{\partial a}{\partial\alpha} = \frac{\partial a}{\partial\beta} \qquad (37)$$

which follows from the right-hand side in (35) being a function of $(\alpha + \beta)$. When (37) is substituted in (36), the result is

$$\sum_{i=1}^N \int_{(i-1)\alpha_0}^{(i-1)\alpha_0 + \alpha'} \delta[a(\alpha,\beta)] \left|1 + \frac{\partial\beta}{\partial\alpha}\right| d\alpha$$
$$= \left|\frac{1}{\partial a/\partial\alpha}\right|_{(\alpha,\beta)=(\alpha_1,\beta_1)} + \left|\frac{1}{\partial a/\partial\alpha}\right|_{(\alpha,\beta)=(\alpha_2,\beta_2)}. \qquad (38)$$

From (35), the partial of $a(\alpha, \beta)$, with respect to α, is given by

$$\frac{\partial a}{\partial\alpha} = -(x'-x)\sin(\alpha+\beta) + (y'-y)\cos(\alpha+\beta). \qquad (39)$$

Equation (38) requires this derivative to be calculated at the two roots of $a(\alpha, \beta)$. From (35), both the roots satisfy the condition

$$\tan(\alpha_j + \beta_j) = -\frac{x'-x}{y'-y}. \qquad (40)$$

Substituting (40) in (39) leads to

$$\left|\frac{\partial a}{\partial\alpha}\right|_{(\alpha,\beta)=(\alpha_1,\beta_1)} = \left|\frac{\partial a}{\partial\alpha}\right|_{(\alpha,\beta)=(\alpha_2,\beta_2)}$$
$$= \sqrt{(x'-x)^2 + (y'-y)^2}. \qquad (41)$$

Substituting (38) and (41) in (34) leads to the final result

$$g(x,y) = \iint f(x',y')\, \frac{1}{\sqrt{(x'-x)^2 + (y'-y)^2}}\, dx'\, dy'. \qquad (42)$$

This relationship can be symbolically expressed as
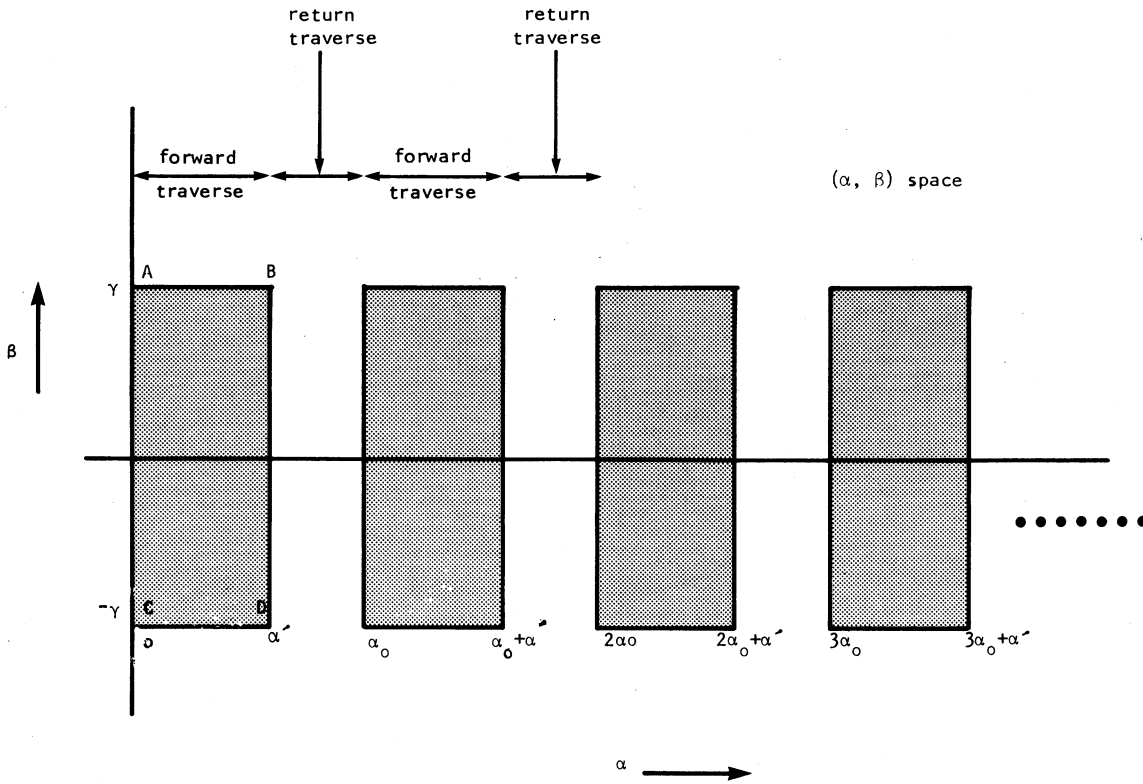
$$g(x,y) = f(x,y) ** \frac{1}{r} \qquad (43)$$

Fig. 12. Shown here are the regions of the (α, β) space that are covered during successive traverses.

where $r = \sqrt{x^2 + y^2}$ and ** indicates two-dimensional convolution. Our final result indicates that when data are collected without any holes or partial overlaps, the traverse-continuous-rotate scanners share with other machines the fundamental property that the point spread function of the backprojection operator is $1/r$.

VI. PROPERTIES OF THE TRANSFORMATION BETWEEN (l, θ) AND (α, β) SPACES

The preceding section utilized the fact that the transformation between (l, θ) and (α, β) spaces is regular (regularity implies one-to-one[5] and onto [8]). The same property is also used in the next section where we will present a convolution-backprojection reconstruction formula. In this section we will prove this property.

A transformation is regular if 1) it is continuous; 2) its partial derivatives are continuous; and 3) the Jacobian of the transformation is nonzero in the region of interest. We will now show that the transformation in (2) satisfies all these conditions. We will only consider the case of constant rota-

[5]The reader might wonder about the property of the transformation being one-to-one, given the fact that (as was mentioned in Section II) the origin within the Radon disk is a point of singularity. Due to $p_\theta(l)$ being multiple valued at the origin, the origin will get transformed into a contour (consisting of many disconnected pieces) in the (α, β) space. This singularity at the origin is merely an artifact of the polar coordinate visualization of the line-integral data. For analytical discussions of the transformations between (l, θ) and (α, β) spaces, the appropriate representation of the (l, θ) space is as shown in Fig. 3(b), and no singularity exists there. However, since the end results remain the same, we will continue to use the polar coordinate representation here.

tional and traverse velocities. In this case, the rotational angle $\alpha(t)$ and the traverse position $S(t)$ are related by the following equation:

$$S(t) = \frac{D}{\alpha'} \left[2(\alpha(t) - (i-1)\alpha_0) - \alpha' \right]$$

$$(i-1)T_t \leqslant t < (i-1)T_t + T_f \quad (44)$$

where α' is the angle of rotation during the forward (left to right) traverse only. Since the forward traverse time is $k/(1+k)$ of the total time for one traverse, α' is given by

$$\alpha' = \frac{k}{1+k} T_t V_a. \quad (45)$$

Substituting (44) in (2), we get

$$\theta = \alpha + \beta$$

$$l = h \sin \beta + \left[\frac{2D}{\alpha'} (\alpha(t) - (i-1)\alpha_0) - D \right] \cos \beta. \quad (46)$$

We already know that in the (l, θ) space the projection data occupy a circular region as shown in Fig. 3. In the (α, β) space, the region occupied by the projection data are as shown in Fig. 12. For example, during the first forward traverse, for each value of α between 0 and α', the angles β range from $-\gamma$ to $+\gamma$ to cover the source fan. During the return traverse, the object rotates from α' to α_0. After that, the collection of the projection data begins again for the second traverse, and so on. This is shown diagrammatically in Fig. 12. During the first traverse, consider the ray given by $\beta = +\gamma$, which is the extreme right ray in the source fan. As α increases from 0 to α_1,
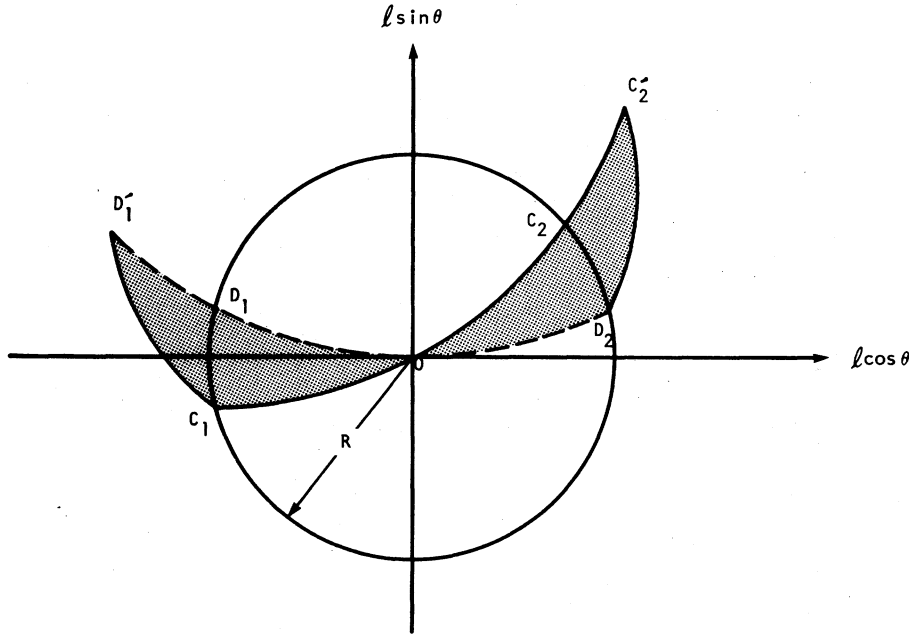
Fig. 13. The shaded area in the Radon space shown here is related by a one-to-one transformation to the first rectangular "box" on the left in Fig. 12.

where α_1 is less than α' and is equal to $V_a T_1$ (see Fig. 9), the track generated in the (l, θ) space is $C_1 O C_2$ shown in Fig. 6. For values of α between α_1 and α', the track generated is a continuation of $C_1 O C_2$ as shown in Fig. 13 by the curve $C_1 O C_2 C_2'$. Similarly, one can show that the line CD in Fig. 12 corresponds to the curve $D_1' D_1 O D_2$ in Fig. 13. Therefore, the shaded area in Fig. 13 corresponds to the first shaded box on the left in Fig. 12. Suppose we assume again, for the sake of diagrammatic representation, that only half the data in each traverse (corresponding to $C_1 O D_1$) are retained for reconstruction, the successive boxes in Fig. 12 will then fill the Radon space as shown in Fig. 14.

Since the transformation equations in (44) are continuous for each region in Fig. 12 and its corresponding region in Fig. 13, and, also, the partial derivations of the equations are continuous in the same regions, in order to prove regularity all we have to prove is that the Jacobian of the transformation does not go to zero.

The Jacobian of the transformation in (46) is given by

$$J = \begin{vmatrix} \dfrac{\partial l}{\partial \alpha} & \dfrac{\partial l}{\partial \beta} \\[2mm] \dfrac{\partial \theta}{\partial \alpha} & \dfrac{\partial \theta}{\partial \beta} \end{vmatrix}. \qquad (47)$$

Using (2) in (47), we obtain

$$J = \left(\frac{2D}{\alpha'} - h\right) \cos \beta + \left(\frac{2D}{\alpha'} \alpha - D\right) \sin \beta \qquad (48)$$

for $0 \leqslant \alpha \leqslant \alpha'$. It can be shown that $J > 0$ provided the following condition is satisfied:

$$\tan\left(\frac{\pi}{2} - \gamma\right) > \left|\frac{D}{(2D/\alpha') - h}\right|. \qquad (49)$$

Therefore, this condition must be satisfied in addition to those in (13).

VII. A CONVOLUTION-BACKPROJECTION RECONSTRUCTION ALGORITHM

The inverse Radon transformation can be represented as a convolution-backprojection integral given by

$$f(x, y) = \int_0^\pi \int_{-R}^{R} p_\theta(l) H(x \cos \theta + y \sin \theta - l) \, dl \, d\theta \qquad (50)$$

where $H(u)$ is the filter function which nominally obeys the following transform property:

$$H(u) = \int |w| \, e^{j2\pi w u} \, dw. \qquad (51)$$

Equation (50) may also be expressed as

$$f(x, y) = \tfrac{1}{2} \int_0^{2\pi} \int_{-R}^{R} p_\theta(l) H(x \cos \theta + y \sin \theta - l) \, dl \, d\theta. \qquad (52)$$

Since the transformation between the Radon space depicted in Fig. 14 and the regions of the (α, β) space shown in Fig. 12 is continuous, one-to-one, and onto, the above integral may be expressed in the (α, β) space by using (2):

$$f(x, y) = \tfrac{1}{2} \sum_{i=1}^{N} \iint_{\text{region } i} q_\alpha(\beta) H[x \cos(\alpha + \beta)$$

$$+ y \sin(\alpha + \beta) - h \sin \beta - S(t) \cos \beta] \, J \, d\beta \, d\alpha \qquad (53)$$

where J is the Jacobian and where region i for the integration corresponds to $D_1' O C_2' D_2 O C_1$ in the Radon space in Fig. 13. In the (α, β) plane, region i is simply the ith shaded box from
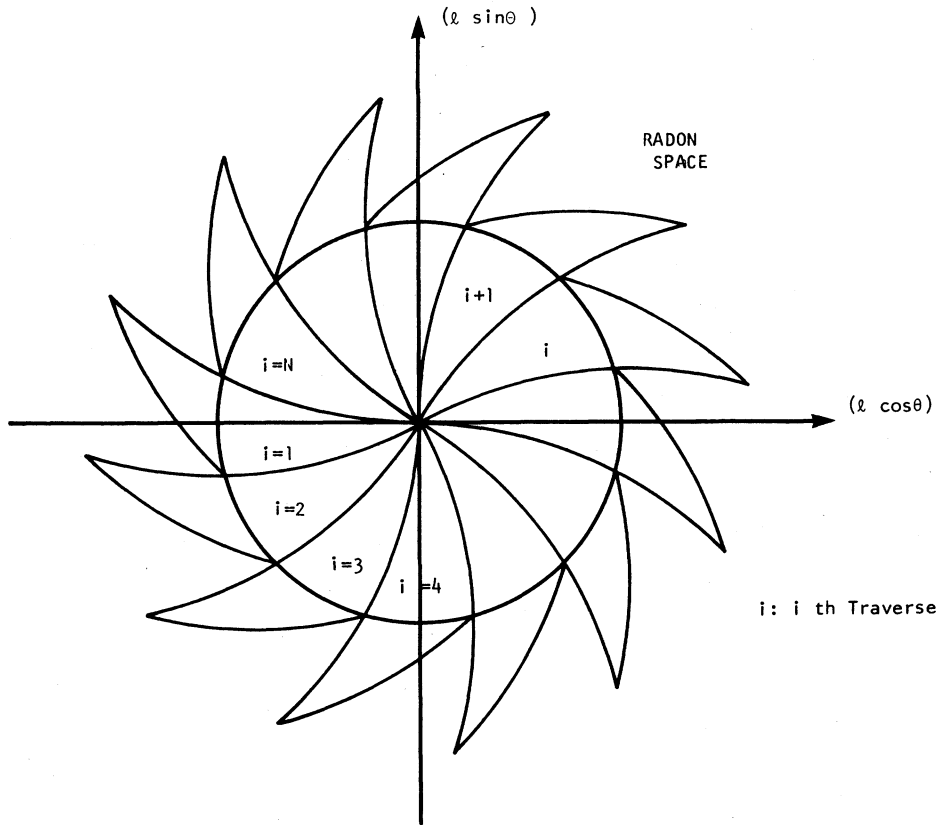
Fig. 14. This figure shows how the Radon space is covered by the different shaded regions in Fig. 12.

the left in Fig. 12. Therefore, the limits of integration may be explicitly stated as follows:

$$f(x, y) = \frac{1}{2} \sum_{i=1}^{N} \int_{(i-1)\alpha_0}^{(i-1)\alpha_0 + \alpha'} \int_{-\gamma}^{\gamma} q_\alpha(\beta) H[x \cos(\alpha + \beta)$$

$$+ y \sin(\alpha + \beta) - h \sin \beta - S(t) \cos \beta] J \, d\beta \, d\alpha. \quad (54)$$

As with the third-generation scanners, it is easier to derive the convolution-backprojection algorithm when the image is expressed in polar coordinates. Using

$$x = r \cos \phi$$

$$y = r \sin \phi \quad (55)$$

we can rewrite (50) as

$$f(r, \phi) = \frac{1}{2} \sum_{i=1}^{N} \int_{(i-1)\alpha_0}^{(i-1)\alpha_0 + \alpha'}$$

$$\cdot \int_{-\gamma}^{\gamma} q_\alpha(\beta) H[L \sin(\beta' - \beta)] J \, d\beta \, d\alpha \quad (56)$$

where

$$L = \sqrt{[r \cos(\alpha - \phi) - S(t)]^2 + [r \sin(\alpha - \phi) + h]^2} \quad (57)$$

and

$$\tan \beta' = \frac{r \cos(\alpha - \phi) - S(t)}{r \sin(\alpha - \phi) + h}. \quad (58)$$

Substituting $u = L \sin \beta$ in (51) and using the transformation

$w' = (wL \sin \beta / \beta)$, we can show that

$$H(L \sin \beta) = \left(\frac{\beta}{L \sin \beta}\right)^2 H(\beta). \quad (59)$$

Substituting (59) in (56) and also using the expression for the Jacobian derived in the preceding section, we get

$$f(r, \phi) = \frac{1}{2} \sum_{i=1}^{N} \int_{(i-1)\alpha_0}^{(i-1)\alpha_0 + \alpha'} \frac{1}{L^2}$$

$$\cdot \int_{-\gamma}^{\gamma} q_\alpha(\beta) W(\alpha, \beta) G(\beta' - \beta) \, d\beta \, d\alpha \quad (60)$$

where the convolution function $G(\beta)$ is given by

$$G(\beta) = \left(\frac{\beta}{\sin \beta}\right)^2 H(\beta) \quad (61)$$

which is the same as that used by the third-generation reconstruction algorithm. The data weight function $W(\alpha, \beta)$ in (60) is given by

$$W(\alpha, \beta) = \left(\frac{2D}{\alpha'} - h\right) \cos \beta + \left[\frac{2D}{\alpha'}(\alpha - (i-1)\alpha_0) - D\right] \sin \beta. \quad (62).$$

A practical implementation of the prefiltering algorithm can be obtained by discretizing the above equations. It is also possible to derive a new set of equations based on a new coordinate system (α, ν), which when discretized will yield detectors that are equally spaced. The two algorithms will be referred

to as equal angle and equal space configurations, respectively. Referring to Fig. 5, the new variable ν is related to β with

$$\nu = h \tan \beta. \tag{63}$$

Following the procedure used to obtain (60), one can derive the reconstruction formula for the equal space configuration:

$$f(r, \phi) = \frac{1}{2} \sum_{i=1}^{N} \int_{(i-1)\alpha_0}^{(i-1)\alpha_0 + \alpha'} \frac{1}{U^2}$$

$$\cdot \int_{-V}^{V} q_\alpha(\nu) H(\nu' - \nu) \overline{W}(\alpha, \nu) \, d\nu \, d\alpha \tag{64}$$

where

$$\nu' = \frac{h[r \cos(\alpha - \phi) - S(t)]}{r \sin(\alpha - \phi) + h}, \tag{65a}$$

$$U = 1 + \frac{r}{h} \sin(\alpha - \phi), \tag{65b}$$

$$V = h \tan \gamma, \tag{65c}$$

and

$$\overline{W} = \frac{(2D/\alpha' - h)h + [2D/\alpha'(\alpha - (i-1)\alpha_0) - D]\nu}{h \sqrt{h^2 + \nu^2}}. \tag{65d}$$

VIII. Computer Simulation Results

In our analytical discussions so far, we have referred to $q_\alpha(\beta)$ as the projection data which, given the entire range of α and β, is indeed correct. In practice, while the continuous traverse and rotation are taking place, one is likely to collect the line integral data by sampling the outputs of the detectors (shown in Fig. 4) at regular time intervals. The readings from all the detectors at a single instant of time will be called one "flash."[6] The number of flashes during each traverse will be denoted by N_{flash}. The symbol N_{det} will denote the number of detectors used (see Fig. 4). The total number of traverses, which in the preceding theoretical analysis was represented by N, will now be denoted by N_{trav}. Note that the line-integral data are collected only during the forward traverses.
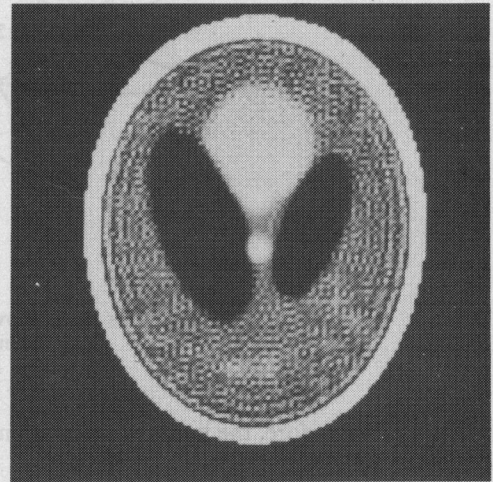
A computer program was written to generate the line-integral data for the Shepp and Logan [10] phantom shown in Fig. 15(a). Because of the limitations on computer time and memory, the number of line-integrals used was small compared to what is typical in industry today. Fig. 15(b) shows a 128×128 reconstruction of the phantom using the convolution-backprojection formula of (64) and (65) with $N_{\text{det}} = 40$, $N_{\text{flash}} = 100$, and $N_{\text{trav}} = 23$. The ringing artifacts caused by

(a)

(b)

(c)

Fig. 15. (a) The Shepp and Logan head phantom. (b) A 128×128 reconstruction of the phantom based on the convolution-backprojection equations (64) and (65) with 40 detectors, 100 flashes in each traverse, and 23 traverses. (c) A median filtered version of the same reconstruction.

the "skull" in the reconstruction are particularly noticeable. They are a manifestation of the bandlimited nature of the discrete implementation of the algorithm [11], [12]. Fig. 15(c) shows a median filtered version of the reconstruction. Median

---

[6] In actuality, of course, the detector readings cannot represent the instantaneous photon flux, but will be equal to its integral over the preceding few milliseconds. We will assume that this integration time at the detector output is short enough so that the rotation of the source-detector gantry during this interval may be ignored. This assumption is also made in the analysis of the third-generation scanner data, where any rotational smearing caused by the nonzero integration time at the detector is usually ignored.
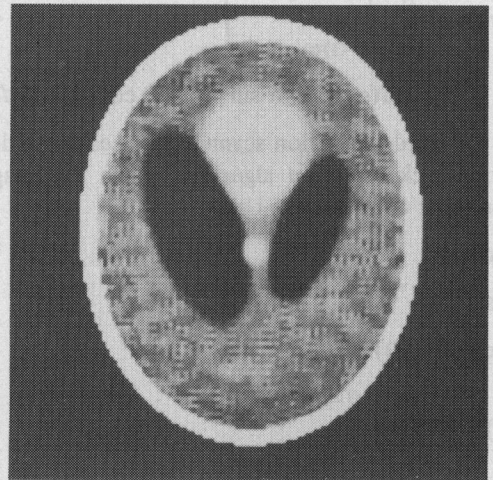
We feel that flash, as opposed to projection, is a better word for the data so collected, since at the instant of measurement the source fan only partially illuminates the object.
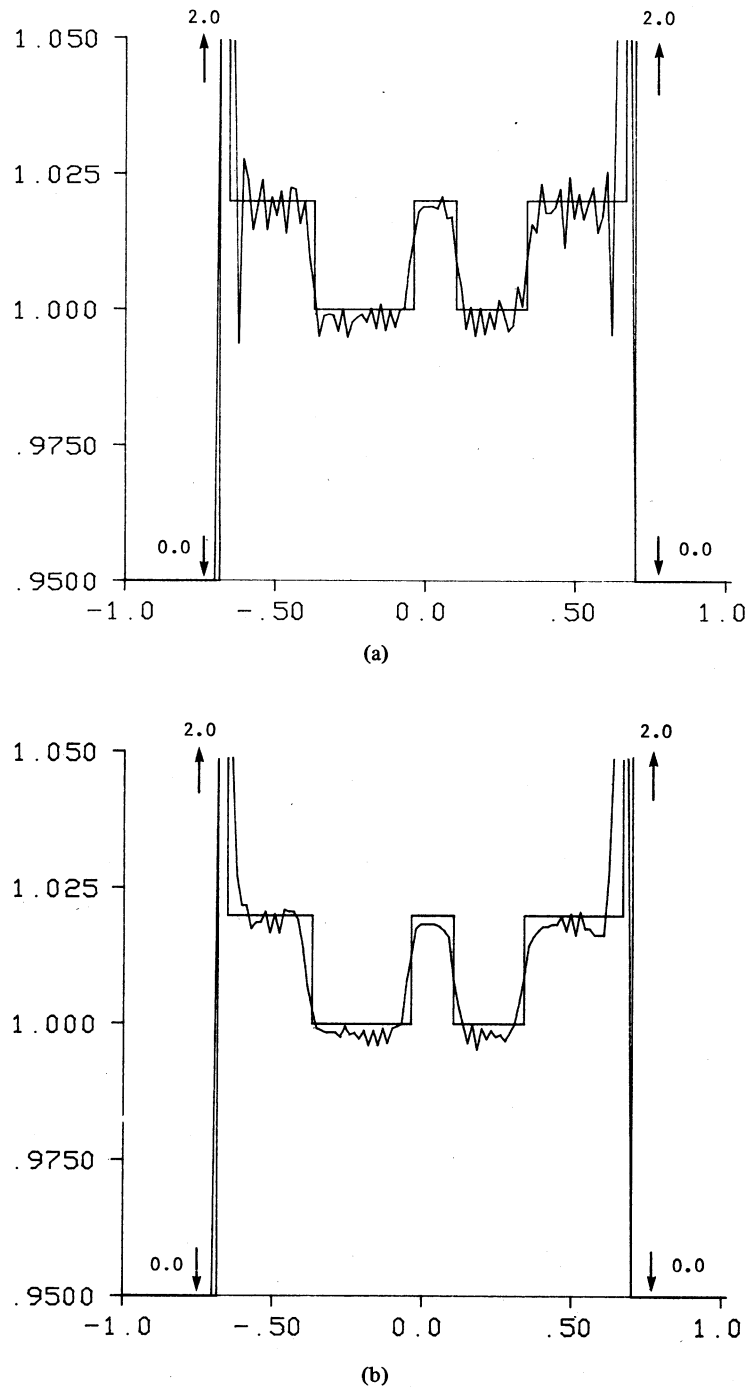
(a)

(b)

Fig. 16. (a) A numerical comparison of the gray levels in the original phantom of Fig. 15(a) and its reconstruction in Fig. 15(b) over the middle horizontal line ($y = 0$). (b) Here the same comparison is shown for the median filtered version in Fig. 15(c).

filtering was done with a 3×3 window. Fig. 16(a) shows a numerical comparison of the original phantom [see Fig. 15(a)] and its reconstruction [see Fig. 15(b)] on a horizontal line passing through the center of the image (this line corresponds to $y = 0$ in [10]). Fig. 16(b) shows the same comparison for the median filtered reconstruction of Fig. 15(c). Fig. 17(a) and (b) corresponds to Fig. 16(a) and (b) for the case of a horizontal line passing through the three very small ellipses near the bottom of the phantom (this line corresponds to

$y = -0.605$ in [10]). It is clear that the number of line integrals used was not adequate to resolve the three ellipses.

Most of the artifacts and noise in the reconstruction in Fig. 15(b) can be attributed to the data collection density (as represented by the chosen values of N_{flash}, N_{det}, and N_{trav}) not being large enough to do adequate justice to the large transitions at the edges of the "skull" (the outermost ring). In Fig. 18(a) is shown the same phantom without this ring. Fig. 18(b) shows its reconstruction using the same N_{flash},
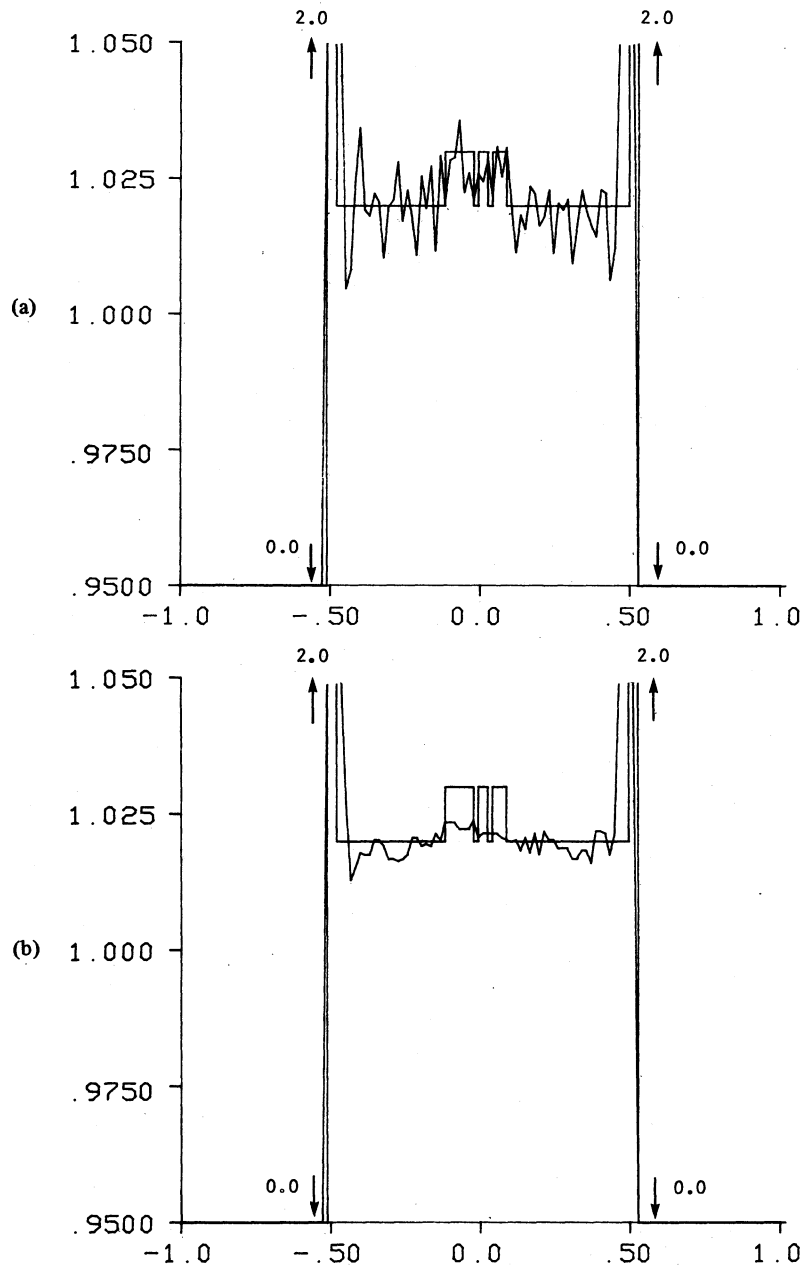
Fig. 17. (a) This figure shows the comparison between the original and
its reconstruction in Fig. 15(b) at the $y = -0.605$ line. (b) The cor-
responding comparison for the median filtered reconstruction.

N_{det}, and N_{trav} as in Fig. 15(b). Fig. 18(c) and (d) shows the
numerical comparisons corresponding to Figs. 16(a) and 17(a)
for the complete phantom.

REFERENCES

[1] A. C. Kak, "Computerized tomography with X-ray, emission, and
ultrasound sources," Proc. IEEE, vol. 67, pp. 1245-1272, Sept.
1979.

[2] A. V. Lakshminarayanan, "Reconstruction from divergent ray
data," Dep. Comput. Sci., State Univ. New York, Buffalo, Tech.
Rep. 92, 1975.

[3] G. T. Herman and A. Naparstek, "Fast image reconstruction
based on a Radon inversion formula appropriate for rapidly col-
lected data," SIAM J. Appl. Math., vol. 33, pp. 511-533, Nov.
1977.

[4] J. Radon, "Uber die Bestimmung von Funktronen durch ihre
Integralwerte Langs gewisser Mannigfaltigkeiten," Ber. Saechsische
Akademie der Wissenschaften, vol. 29, pp. 262-277, 1917.

[5] I. M. Gel'fand, M. I. Graev, and N. Ya. Vilenkin, Generalized
Functions, vol. 5. New York: Academic, 1966, ch. 1.

[6] P. R. Smith, T. M. Peters, and R. H. T. Bates, "Image reconstruc-
tion from finite numbers of projections," J. Phys. A: Math. Nucl.
Gen., vol. 6, pp. 361-382, Mar. 1973.

[7] G. T. Gullberg, "The reconstruction of fan-beam data by filtering
the back-projection," Comput. Graphics and Image Proc., vol. 10,
pp. 30-47, 1979.

[8] W. H. Fleming, Functions of Several Variables. New York:
Addison-Wesley, 1965.

[9] A. Papoulis, System and Transforms with Applications in Optics.
New York: McGraw-Hill, 1968, p. 38.

[10] L. A. Shepp and B. F. Logan, "The Fourier reconstruction of a
head section," IEEE Trans. Nucl. Sci., vol. NS-21, pp. 21-43,
1974.

[11] C. R. Crawford and A. C. Kak, "Aliasing artifacts in computer-
ized tomography," Appl. Opt., vol. 18, pp. 3704-3711, Nov.
1979.

[12] G. H. Weiss and R. A. Brooks, "Integration errors in image recon-
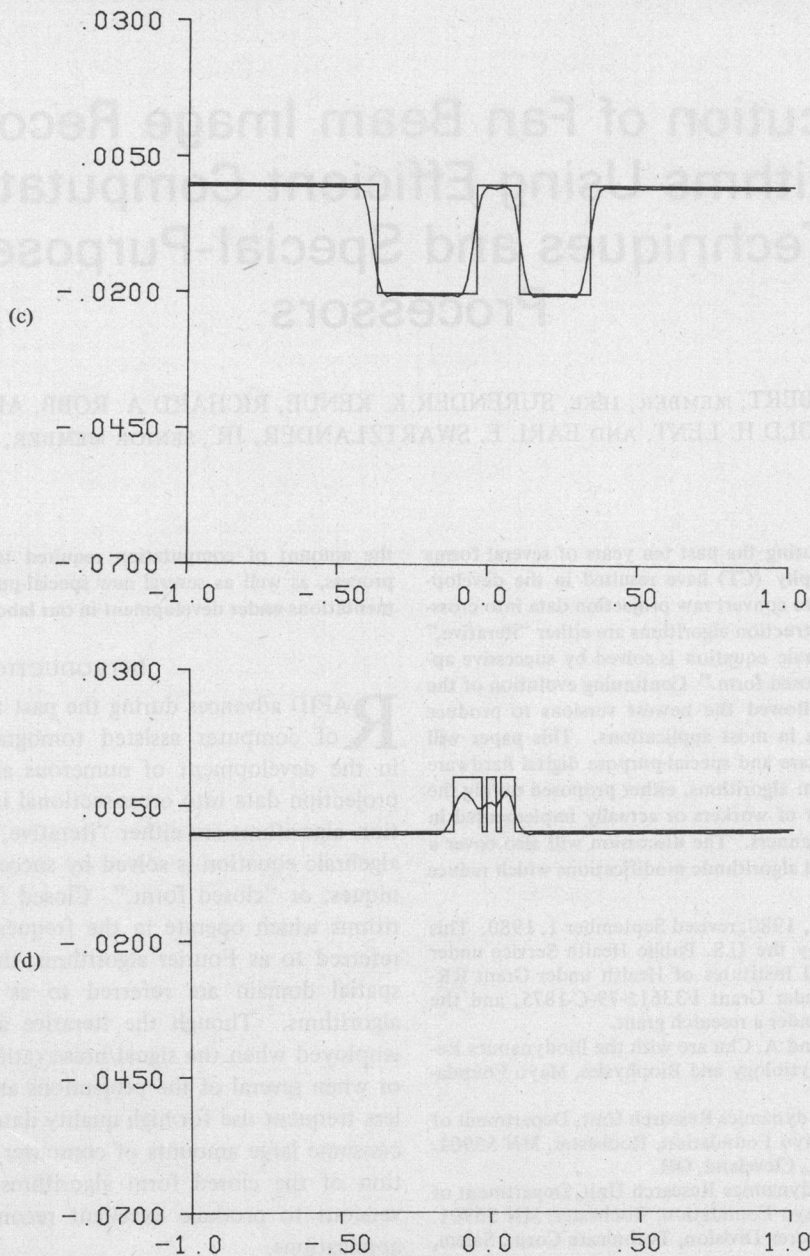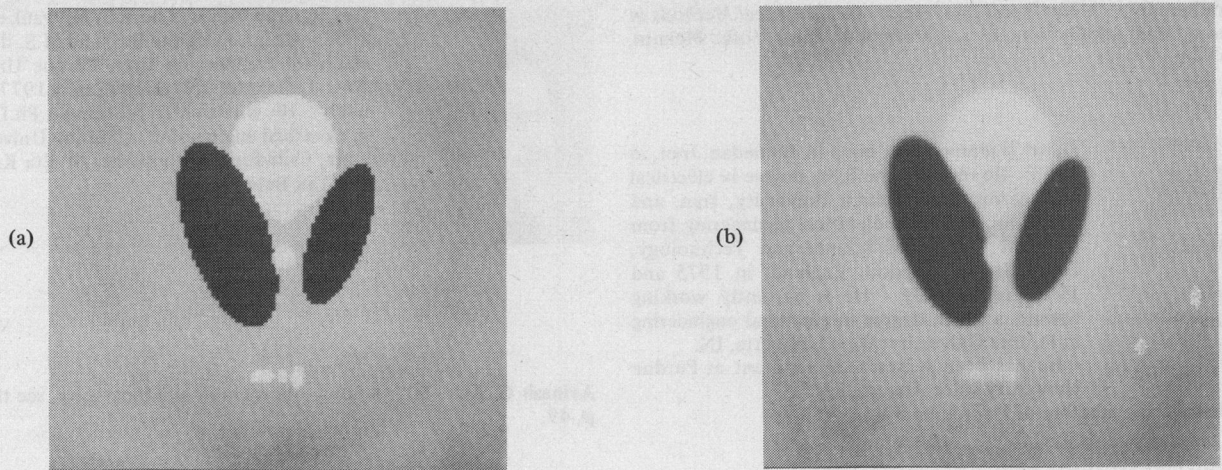struction of circularly symmetric objects in computer assisted

Fig. 18. (a) Shown here is the phantom without the outer ring. (b) A reconstruction of (a) with the same N_{flash}, N_{det}, and N_{trav} as in Fig. 15(b). (c) A numerical comparison corresponding to Fig. 16(a). (d) A numerical comparison corresponding to Fig. 17(a).

tomography," in *Statistical Mechanics and Statistical Methods in Theory and Application*, U. Landman, Ed. New York: Plenum, 1977.
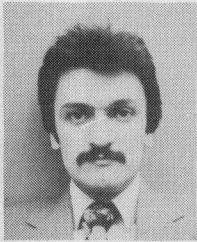
David Nahamoo was born in Hamedan, Iran, in 1953. He received the B.Sc. degree in electrical engineering from Tehran University, Iran, and the M.Sc. degree in electrical engineering from Imperial College of Science and Technology, University of London, England, in 1975 and 1976, respectively. He is currently working toward a Ph.D. degree in electrical engineering at Purdue University, West Lafayette, IN.

He has been a Research Assistant at Purdue University since August, 1977.

Mr. Nahamoo is a member of Phi Kappa Phi.

Carl R. Crawford was born in Milwaukee, WI, in 1956. He received the B.S. and M.S. degrees in electrical engineering from Purdue University, West Lafayette, IN, in 1976 and 1977, respectively. He is currently pursuing a Ph.D. degree in electrical engineering at Purdue University.

Mr. Crawford is a member of Eta Kappa Nu and Tau Beta Pi.

Avinash C. Kak (M'71), for a photograph and biography, see this issue, p. 49.

Rapid Execution of Fan Beam Image Reconstruction Algorithms Using Efficient Computational Techniques and Special-Purpose Processors

BARRY K. GILBERT, MEMBER, IEEE, SURENDER K. KENUE, RICHARD A. ROBB, ALOYSIUS CHU, ARNOLD H. LENT, AND EARL E. SWARTZLANDER, JR., SENIOR MEMBER, IEEE

Abstract—Rapid advances during the past ten years of several forms of computer-assisted tomography (CT) have resulted in the development of numerous algorithms to convert raw projection data into cross-sectional images. These reconstruction algorithms are either "iterative," in which a large matrix algebraic equation is solved by successive approximation techniques; or "closed form." Continuing evolution of the closed form algorithms has allowed the newest versions to produce excellent reconstructed images in most applications. This paper will review several computer software and special-purpose digital hardware implementations of closed form algorithms, either proposed during the past several years by a number of workers or actually implemented in commercial or research CT scanners. The discussion will also cover a number of recently investigated algorithmic modifications which reduce the amount of computation required to execute the reconstruction process, as well as several new special-purpose digital hardware implementations under development in our laboratories at the Mayo Clinic.

INTRODUCTION

RAPID advances during the past ten years of several forms of computer assisted tomography (CT) have resulted in the development of numerous algorithms to convert raw projection data into cross-sectional images. These reconstruction algorithms are either "iterative," in which a large matrix algebraic equation is solved by successive approximation techniques; or "closed form." Closed form reconstruction algorithms which operate in the frequency domain are generally referred to as Fourier algorithms; those which operate in the spatial domain are referred to as filtered back projection algorithms. Though the iterative algorithms are frequently employed when the signal/noise ratio of the input data is low, or when several of the projections are unavailable, they are in less frequent use for high quality data, since iterative solutions consume large amounts of computer time. Continuing evolution of the closed form algorithms has allowed the newest versions to produce excellent reconstructed images in most applications.

This paper will review several computer software and special-purpose digital hardware implementations of closed form